

Photon Dominated Regions in NGC3603

[CI] and mid-J CO line emission

M. Röllig¹, C. Kramer², T. Minamidani⁴, K. Sun², R. Simon², M. Cubick², M. Hitschfeld², M. Aravena¹, F. Bensch¹,
F. Bertoldi¹, L. Bronfman⁶, M. Fujishita⁵, Y. Fukui³, U.U. Graf², N. Honingh², S. Ito³, H. Jakob², K. Jacobs²,
U. Klein¹, B.-C. Koo⁶, J. May⁴, M. Miller², Y. Miyamoto³, N. Mizuno³, T. Onishi³, Y.-S. Park⁷, J. Pineda¹,
D. Rabanus², H. Sasago³, R. Schieder², J. Stutzki¹, H. Yamamoto³, and Y. Yonekura⁵

¹ Argelander-Institut für Astronomie *, Universität Bonn, Auf dem Hügel 71, D-53121 Bonn, Germany

² I. Physikalisches Institut, Universität zu Köln, Zùlpicher Str. 77, D-50937 Köln, Germany

³ Department of Astrophysics, Nagoya University, Chikusa-ku, Nagoya 464-8602, Japan

⁴ Department of Physics, Hokkaido University, Kita-ku, Sapporo 060-0810, Japan

⁵ Department of Physical Science, Osaka Prefecture University, Osaka 599-8531, Japan

⁶ Departamento de Astronomía, Universidad de Chile, Casilla 36-D, Santiago, Chile

⁷ Seoul National University, Seoul 151-742, Korea

Preprint online version: September 18, 2007

ABSTRACT

Aims. We aim at deriving the excitation conditions of the gas as well as the local FUV intensities to get a coherent picture of how the gas in NGC 3603 is energized by the central stars.

Methods. The NANTEN2-4m submillimeter telescope is used to map [CI] 1.0, 2.1 and CO 4.3 and 7.6 lines in a $2' \times 2'$ region around the central OB cluster HD 97950 in NGC 3603. These data are combined with C¹⁸O 2–1 data, HIRES/-processed IRAS 60 μ m and 100 μ m maps of the FIR continuum, and maps of IRAC on Spitzer.

Results. We used the HIRES far-infrared dust data to create a map of the FUV field heating the local dust. We can constrain the FUV field to values of $\chi = 5 - 20 \times 10^3$ in units of the Draine field. Despite the large number of very massive O and WNL stars, the FUV field illuminating the PDR is less intense than in the Orion Nebula because the interface is further away from the illuminating stars. Applying LTE and escape probability approximations, we can derive temperatures ($T_{\text{MM1}} = 26$ K, $T_{\text{MM2}} = 47$ K), column densities ($N_{\text{MM1}} = 1.6 \times 10^{22}$ cm⁻², $N_{\text{MM1}} = 2 - 5 \times 10^{22}$ cm⁻²) and densities ($n_{\text{MM1}} \geq 10^{5.5}$, $n_{\text{MM2}} \geq 10^5$) for the two observed molecular clumps MM1 and MM2.

Conclusions. ...?

Key words. ISM: clouds

1. Introduction

Understanding the feedback between star formation and the interstellar medium (ISM) is important in order to understand the process of star formation. The physical and chemical properties of stars are the heritage of their parental clouds. Stars are born from interstellar gas and release metal-enriched material to the ISM when they die. Radiation from the stars is the prime heating source for gas and dust in nearby molecular clouds and may additionally trigger velocity and density fluctuations, that stimulate further star formation. To understand the formation of these next generation stars, it is important

to understand how the previous generation interacts with its parental clouds. The energy incident on the clouds in the form of stellar far ultraviolet (FUV: $6 \text{ eV} \leq h\nu \leq 13.6 \text{ eV}$) radiation is countered by cooling emission of atomic fine-structure lines ([CI]370 μ m, 610 μ m, and [OI]63 μ m, 145 μ m) and by molecular rotational lines (CO, H₂O, OH, etc.). The cooling emission carries the imprint of the local physical and chemical conditions and can be used to infer the type of environment conducive to maintaining star formation. On their way into a molecular cloud, FUV photons are absorbed, and a depth-dependent chemical balance is established. Models of these so-called photon dominated regions (PDRs) typically predict a stratification of species like H/H₂, C⁺/C/CO, and others. This stratification is found to be independent of the shape of the PDR (e.g. Gorti & Hollenbach 2002). However, observations often reveal [CI] emission coincident with that of CO (e.g. Tatematsu

Send offprint requests to: M. Röllig,

e-mail: roellig@astro.uni-bonn.de

* Founded by merging of the Sternwarte, Radi astronomisches Institut and Institut für Astrophysik und Extraterrestrische Forschung

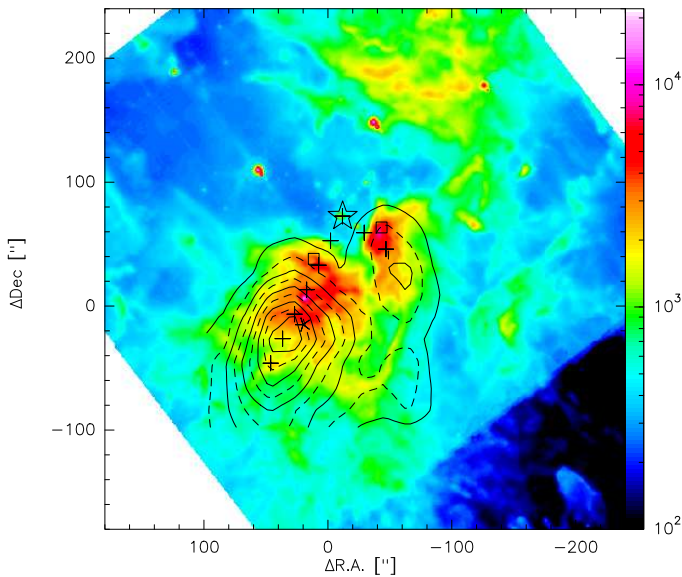


Fig. 1. 8 μm Spitzer/IRAC band (in MJy/sr) overlaid with CO 4–3 NANTEN2 observations presented in this paper. The position of the cluster is marked by the star. The boxes mark the position of the pillar heads. The crosses mark the positions along the cuts into MM1 and MM2. Irac pixel size is 1.2''.

et al. 1999; Ikeda et al. 2002; Sakai et al. 2006). Plane-parallel models cannot explain this behavior unless full face-on orientation is assumed. Spherical models under isotropic illumination show well-correlated [CI] and CO emission for low density clouds ($n \lesssim 10^4 \text{cm}^{-3}$) but predict a limb brightening of the [CI] emission. In this work we analyze the distribution of atomic carbon and warm CO in the NGC3603 star forming region and use PDR models to derive the excitation conditions of the gas.

2. The NGC 3603 star forming region

NGC 3603 is located in the Carina spiral arm ($l \approx 291.6^\circ$, $b \approx -0.5^\circ$) at a distance of about 6 kpc (Stolte et al. 2006). It is one of the most luminous ($L_{\text{bol}} > 10^7 L_\odot$), optically visible HII regions in the Galaxy, with the massive OB cluster NGC 3603 YC (Young Cluster) as a power source (Goss & Radhakrishnan 1969). The compact core of the cluster was designated HD 97950 due to its star-like appearance. As a comparison, NGC 3603 is 100 times more luminous than the Orion Nebula. This young cluster can be considered a one of the few Galactic starburst clusters, which are essential for the understanding of extragalactic star formation. With a stellar cluster mass of $\approx 10^4 M_\odot$ residing in a cloud of total gas mass of $4 \times 10^5 M_\odot$ (Grabelsky et al. 1988), it is the most compact Galactic star-forming regions outside the Galactic center region (Stolte et al. 2004). To the south of the cluster is a giant molecular cloud (see Figure 1). The intensive radiation and fast stellar winds from the cluster are excavating large gaseous pillars (Brandner et al. 2000). Furthermore, CS observations by Nürnbergger et al. (2002) show that the molecular environment also extends much further to the north ($> 10'$), hosting numerous massive molecular clumps.

3. Observations

We used the NANTEN2-4m telescope at 4865m altitude at Pampa la Bola in northern Chile to map the central $2' \times 2'$ region of NGC3603. We observed the rotational transitions of ^{12}CO $J=4 \rightarrow 3$ (461.0408 GHz) and $J=7 \rightarrow 6$ (806.6517 GHz) and the two fine-structure transitions of atomic carbon [CI], $^3\text{P}_1\text{-}^3\text{P}_0$ (492.1607 GHz) and $^3\text{P}_2\text{-}^3\text{P}_1$ (809.3446 GHz) (henceforth 1-0 and 2-1), between September and November 2006 with a dual-channel 460/810 GHz receiver. The exact line frequencies were taken from the *Cologne Database for Molecular Spectroscopy* CDMS (Müller et al. 2005, 2001). Double side-band (DSB) receiver temperatures were ≈ 250 K in the lower frequency channel and ≈ 750 K in the upper channel. The intermediate frequencies (IF) are 4 GHz and 1.5 GHz, respectively. The latter IF allows simultaneous observations of the CO 7–6 line in the lower sideband and the [CI]2–1 line in the upper sideband. These two lines were observed with one of the two lower lines in the 460 GHz channel. As backends, we used two acousto optical spectrometers (AOS) with bandwidths of 1GHz. The channel resolution was 0.37 km s^{-1} at 460 GHz and 0.21 km s^{-1} at 806 GHz. The pointing accuracy was checked regularly on Jupiter, IRC+10216, and IRC2 in OrionA. The applied corrections were always $< 20''$ and usually $< 10''$. To determine the atmospheric transmission, we measured the atmospheric emission at the reference position (RA_{J2000.0} = 11:15:08.85, Dec_{J2000.0} = -61:16:50). Spectra of the two frequency bands were calibrated separately, and side-band imbalances were corrected using the atmospheric model *atm* (Atmospheric Transmission at Microwaves, cf. Pardo et al. 2001). Observations were taken on-the-fly (OTF), scanning in right ascension at a speed of $2.5''/\text{sec}$ and sampling every $10''$. The reference position was observed at the beginning of each OTF scanning line.

Our reference position is RA_{J2000.0} = 11:15:08.85, Dec_{J2000.0} = -61:16:50, $73''$ south-east of the central OB cluster (HD97950) at RA_{J2000.0} = 11:15:07.26, Dec_{J2000.0} = -61:15:37.48. The half power beam widths (HPBW) deconvolved from the observed full widths at half maxima (FWHM) are $38.0''$ and $26.5''$, in the lower and upper receiver bands respectively. Beam efficiencies B_{eff} are 50% and 45%, respectively (Simon et al. 2007). The forward efficiency, $F_{\text{eff}} = 86\%$ in both bands, was determined from skydips. The raw data were calibrated to antenna temperatures T_A^* and scaled to main beam temperatures T_{mb} with the factor $F_{\text{eff}}/B_{\text{eff}}$. We present all data in units of T_{mb} . Second order polynomial baselines were subtracted from all spectra. A few positions required higher order (up to 5th order) baselines to be subtracted. **MOVE Along the two cuts all [CI](2–1) and few (1–0) spectra showed strong standing wave patterns. We corrected for standing waves by subtracting sinusoidal baselines.** About 36% of the total power is detected in at least two error beams (for details see Simon et al. 2007; Kramer et al. 2007)

4. Data

4.1. Dust and PAHs

In Fig.1 we show a map of integrated CO 4–3 intensities from NANTEN2 overlaid on an $8\mu\text{m}$ image taken with the Infrared Array Camera (IRAC) on board the Spitzer space telescope¹. The position of the OB cluster is marked by a star. The image shows prominent molecular clouds southwest and southeast of the cluster position. Following Nürnberger et al. (2002), we refer to them as MM1 and MM2, respectively. The IRAC images show the sharp PDR interfaces between the HII region and the molecular cloud. The positions of these interfaces match the pillar-like structures observed in HST and VLT images (Brandner et al. 2000)(ADD MORE). We also note a dusty filament, which connects MM1 and MM2 in a large arc $1.5'$ to $2'$ south of the western pillar head. This filament is also visible as a slight enhancement ($\approx 80\text{ K}\cdot\text{km/s}$) in the CO 4–3 emission to the southwest. The strong $8\mu\text{m}$ emission ($> 10^4\text{ MJy/sr}$) is due to the FUV flux produced by the OB cluster heating the gas and dust in the molecular clouds. The $8\mu\text{m}$ band, which includes strong PAH emission ($7.6, 7.8,$ and $8.6\mu\text{m}$), traces the PDR interface especially well.

4.2. NANTEN2 observations

4.2.1. Maps of integrated intensity

Fig. 2 shows maps of integrated CO 4–3, 7–6, [C I] 1–0, and 2–1 emission. The OB cluster position is marked by a star. The two molecular clumps MM1 and MM2 are visible: MM1 to the southwest of the OB cluster and MM2 to the southeast. The peak intensities are $285\text{ K}\cdot\text{km s}^{-1}$ for CO 4–3, $129\text{ K}\cdot\text{km s}^{-1}$ for CO 7–6, $29\text{ K}\cdot\text{km s}^{-1}$ for [C I] 1–0, and $24\text{ K}\cdot\text{km s}^{-1}$ for [C I] 2–1. MM2 is very prominent in all 4 observed transitions while MM1 is weaker in [C I] 1–0, and clearly visible in the other three transitions.

Both CO maps show the transition from the HII region to the molecular cloud, especially for MM2. MM1 presumably is smaller than our beam size (Nürnberger et al. 2002), hence it is not possible to infer detailed structure information from the maps. The peak positions of CO 4–3, 7–6, and [C I] 2–1 match very well, while the peak of the [C I] 1–0 emission is shifted ($15''$) to the south-east. However we note a very good spatial correlation between the CO and [C I] emission. All peaks coincide within a beam radius. We cannot confirm the existence of a standard C-CO layering as expected from simple edge-on plane-parallel PDR scenarios. It is possible to explain coincident [C I] and CO emission with a face-on configuration, but the plainly visible pillar structures in the HST observations and the very sharp interface visible in the IRAC image in Fig.1 clearly show a prominent, edge-on PDR interface. The velocity structure of the observed field is shown in the CO 4–3 velocity channel maps (Fig. 3). From the channel maps, it is obvious that the emission in MM1 shows a smaller

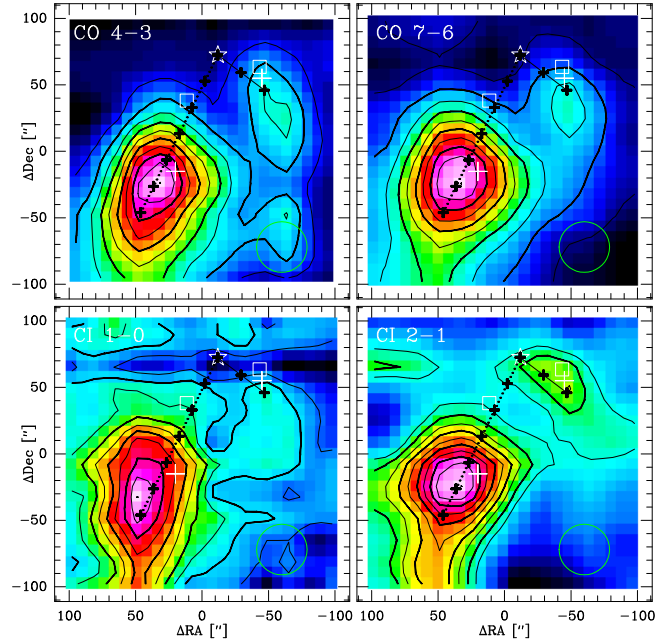


Fig. 2. Velocity integrated maps ($200''\times 200''$) of CO 4–3, 7–6, [C I] 1–0, and 2–1 smoothed to a common angular resolution of $38''$ (1.1 pc at 6 kpc), and integrated over a velocity range from 6 to 26 km s^{-1} . Colorscale and contours show the same data. Contours range between 10 and 90% of the peak intensities which are $285\text{ K}\cdot\text{km s}^{-1}$ for CO 4–3, $129\text{ K}\cdot\text{km s}^{-1}$ for CO 7–6, $29\text{ K}\cdot\text{km s}^{-1}$ for [C I] 1–0, and $24\text{ K}\cdot\text{km s}^{-1}$ for [C I] 2–1. The position of the compact OB cluster is marked by a white star. The position of the pillars, as seen in the HST images, are marked by white squares. Dashed lines and small crosses spaced by $22''$ mark two cut from the OB cluster to the peak positions of the two clumps MM1 (short cut) and MM2 (long cut). The circle marks the resolution and the two white crosses mark the position of the CS(2–1) peaks (Nürnberger et al. 2002) in MM1 and MM2.

kinematic range than MM2. MM1 is not observable at velocities redder than 16 km s^{-1} , while the emission in MM2 extends up to 21 km s^{-1} . At larger velocities, the emission gradually shifts to the southwest.

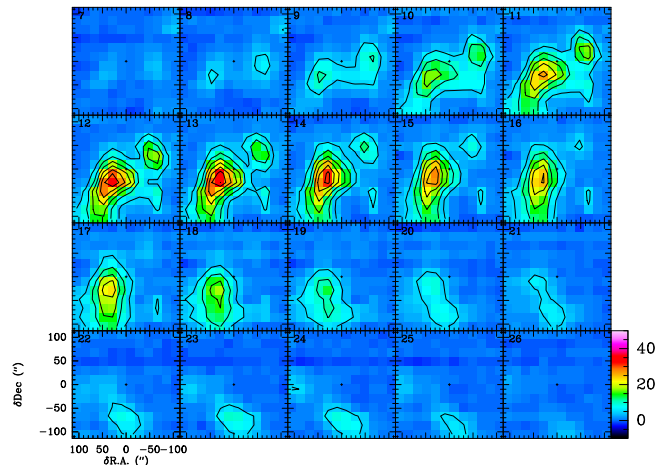


Fig. 3. Velocity structure of the observed field: CO 4–3 velocity channels of 1 km s^{-1} width. Contours range between 5 and $45\text{ K}\cdot\text{km s}^{-1}$ in steps of $5\text{ K}\cdot\text{km s}^{-1}$.

¹ These post-BCD data were retrieved from the Spitzer archive (URL <http://archive.spitzer.caltech.edu/>). Because of strong saturation effects, we chose the short exposure data.

Table 1. Observed integrated intensities $I = \int T_{\text{mb}} dv$ in units of $\text{K}\cdot\text{km s}^{-1}$, v_{LSR} in units of km s^{-1} , and the line widths FWHM in units of km s^{-1} computed as 0th, 1st, and 2nd moment of the spectra between $v = 8\text{--}22 \text{ km s}^{-1}$. The positions lie along a line starting from the OB cluster. The cluster position has been omitted. Rotational transitions of CO are denoted 43 ($^{12}\text{CO } 4\text{-}3$) and 76 ($^{12}\text{CO } 7\text{-}6$). The atomic carbon fine-structure transitions are denoted 10 ($^3P_1 - ^3P_0$) and 21 ($^3P_2 - ^3P_1$).

$\Delta\alpha/\Delta\delta$ [" / "]	I_{43} [K·km/s]	Δv_{43} [km/s]	v_{LSR} [km/s]	I_{76} [K·km/s]	Δv_{76} [km/s]	v_{LSR} [km/s]	I_{10} [K·km/s]	Δv_{10} [km/s]	v_{LSR} [km/s]	I_{21} [K·km/s]	Δv_{21} [km/s]	v_{LSR} [km/s]
10/30	55	6.2	13.6	31	7.5	13.7	8	8.4	14.7	0	0.0	1.8
20/10	154	6.9	13.9	76	7.0	13.4	14	9.0	14.3	8	3.7	14.5
30/-10	273	7.7	14.4	128	7.3	13.7	24	6.0	14.9	22	4.7	14.8
40/-30	303	8.3	14.3	132	7.8	13.8	29	6.3	14.3	24	5.9	14.0
50/-50	232	7.5	13.8	93	7.7	13.9	24	7.0	14.1	14	4.2	13.6
-30/60	49	7.1	13.6	25	7.6	13.5	2	0.0	25.8	5	5.8	14.6
-50/50	93	5.8	13.3	41	7.0	13.4	10	8.3	12.9	7	4.6	13.1

4.2.2. Spectra along a cut through the region

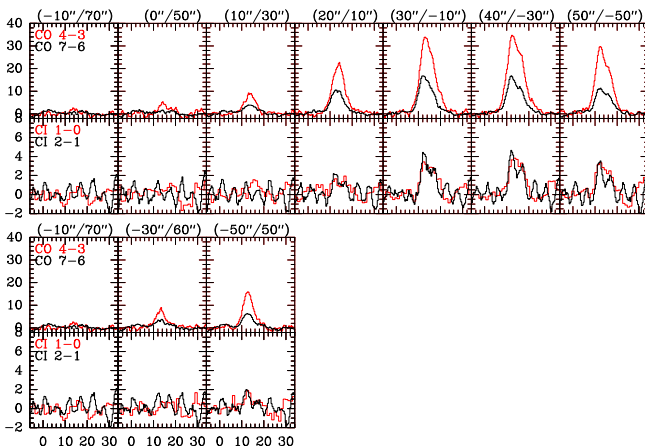


Fig. 4. Spectra along two cut connecting the OB cluster and the centre of MM1 (bottom) and MM2 (top). All data are at a common resolution of $38''$ and on the main beam scale.

The spectra along the two cuts to the peak positions in MM1 and MM2, shown in Fig.4, show the kinematic structure of the interface regions and the molecular clumps. The spectra at the positions $30''/-10''$, $40''/-30''$, and $50''/-50''$ do not show simple Gaussian line profiles. Nürnberger et al. (2002) observed similar line profiles in their CS 3–2 and 2–1 observations of MM2. They used two Gaussian components separated by 3 km s^{-1} to fit the emission profiles. Our analysis showed that it is not possible to use a similar two component Gaussian fit to reproduce our observations at all positions. We derived the first three moments of the spectral line, i.e. integrated intensity, mean velocity, and FWHM, over the channels in the range $v = 6 - 22 \text{ km s}^{-1}$. At the offsets $-10''/70''$ and $0''/50''$ we don't find sufficient emission to apply any reasonable analysis, and we omit these two positions in the following. The derived moments are given in Table 1.

4.3. Analysis

4.3.1. LTE – Column densities and temperatures

In Table 2 we give the line ratios R_{74} (I_{76}/I_{43}), R_{21} (I_{21}/I_{10}) and R_{14} (I_{10}/I_{43}) for all positions along the two cuts. We computed the LTE temperatures using the optically thick CO 4–3 emission. We derive temperatures of $\approx 45 \text{ K}$ for the peak position in MM2 and $\approx 25 \text{ K}$ for MM1. This is consistent with estimates from the [C I] line ratio. R_{21} is a sensitive function of the [C I] excitation temperature. In the optically thin limit and assuming LTE, $T_{\text{ex}} = 38.3 \text{ K} / \ln[2.11/R_{21}]$. In MM2 we find ratios between 0.6 and 0.9 which correspond to temperatures between 30 and 45 K. NOT VALID FOR ALL POINTS. MAYBE REMOVE CS POSITION AT ALL. For MM1 the [C I] line ratio gives a temperature estimate of $\approx 33 \text{ K}$. We then used the excitation temperature to compute the column density of atomic carbon under the assumption of LTE and optically thin emission. The results are also given in Table 2.

We estimate dust temperatures from the ratio of HIREs $60 \mu\text{m}$ and $100 \mu\text{m}$ data, assuming blackbody emission with a spectral index of 1.5 for the dust. For temperatures below 100 K the dust temperature can be approximated according to $T_D = -87.4 / \ln(2.149^{-4} R_{60/100})$. Along the two cuts we find almost constant dust temperatures of 25 K and 27 K for MM1 and MM2, respectively. These temperatures are only rough estimates, of the cool dust because of large beam filling effects.

To derive the total column densities we use the integrated intensity of $\text{C}^{18}\text{O } 2\text{-}1$ as presented in Nürnberger et al. (2002). Assuming an isotope ratio of 500 and $\text{CO}:\text{H}_2 = 8 \times 10^{-5}$ (Frerking et al. 1982), i.e. an assumed ratio of $\text{C}^{18}\text{O}/\text{H}_2 = 2 \times 10^{-7}$, we compute the column densities along the two cuts. For MM1, we find a total column density of $1.6 \times 10^{22} \text{ cm}^{-2}$; for MM2, $N = 2\text{--}5 \times 10^{22} \text{ cm}^{-2}$. Table 2 summarizes the results and also gives the ratio $N(\text{C})/N_{\text{tot}}$. We find that the relative abundance of atomic carbon drops towards the peak positions with values of 9.3×10^{-6} (MM1) and $6.9 - 7.8 \times 10^{-6}$ (MM2) and increases at positions towards as well as away from the OB cluster. **Even though the spatial resolution of our maps is rather coarse, this could be an indication for a C/CO stratification, because in this case we would expect limb brightened [C I] emission.**

Table 2. Line ratios R_{74} (I_{76}/I_{43}), R_{21} (I_{21}/I_{10}) and R_{14} (I_{10}/I_{43}) for all positions along the two cuts. The LTE excitation temperature is derived from the optically thick I_{43} emission. The C column densities are derived under the assumption of LTE and optically thin [C I] emission. REPHRASE CAPTION!!!! Values of the integrated intensities of $C^{18}O$ 2–1 as presented in Nürnberg et al. (2002) along the two cuts, the LTE excitation temperature as derived from I_{43} , the LTE column densities of $C^{18}O$, and the total gas column density, assuming an isotope ratio of 500 and $CO:H_2=8\times 10^{-5}$ (Frerking et al. 1982), i.e. an assumed ratio of $C^{18}O/H_2=2\times 10^{-7}$.

$\Delta\alpha/\Delta\delta$ ["/"]	R_{74}	R_{21}	R_{14}	T_{ex} [K]	$N(\text{C})$ cm^{-2}	$\int T_{\text{mb}}(C^{18}O)dv$ [K km s $^{-1}$]	$N_{C^{18}O}$ [10^{15}cm^{-2}]	N_{tot} [10^{21}cm^{-2}]	$N(\text{C})/N_{\text{tot}}$
10/30	0.56	0.04	0.15	18	1.28×10^{17}	1.6	1.89	9.47	1.4×10^{-5}
20/10	0.50	0.63	0.09	32	1.91×10^{17}	1.9	3.5	17.5	1.1×10^{-5}
30/-10	0.47	0.90	0.09	46	3.59×10^{17}	4.2	10.4	51.8	6.9×10^{-6}
40/-30	0.44	0.85	0.10	47	4.21×10^{17}	4.3	10.8	54.1	7.8×10^{-6}
50/-50	0.40	0.59	0.11	41	3.48×10^{17}	2.1	4.75	23.7	1.5×10^{-5}
-30/60	0.52	2.72	0.04	15	1×10^{17}	1.3	1.41	7.05	1.4×10^{-5}
-50/50	0.45	0.68	0.12	26	1.51×10^{17}	2.1	3.23	16.2	9.3×10^{-6}

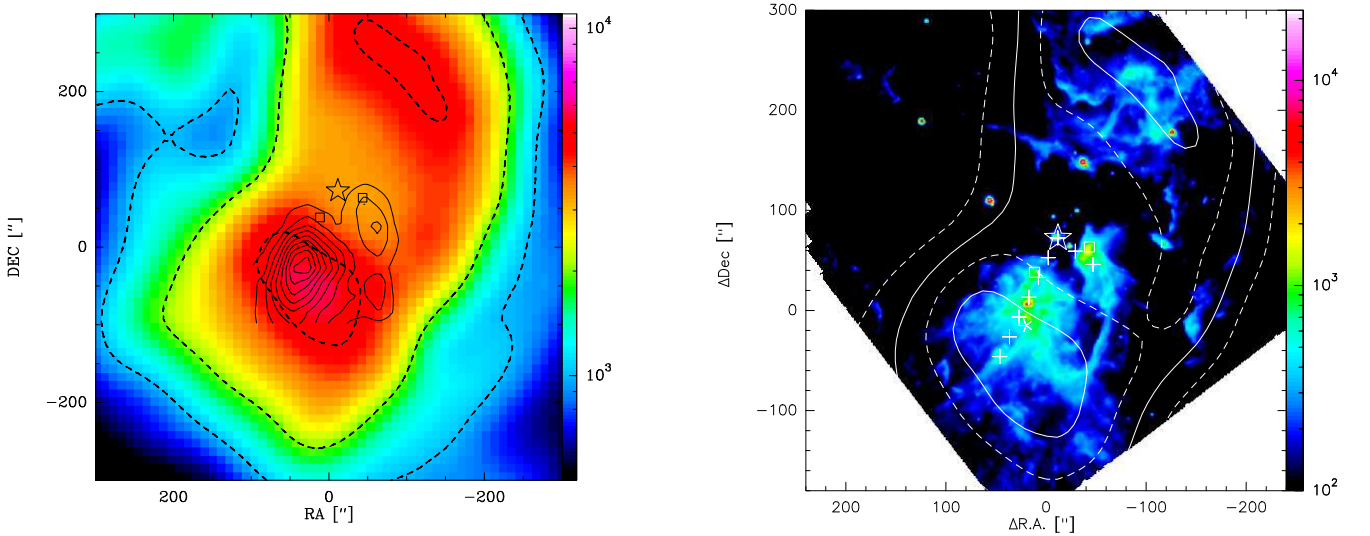


Fig. 5. **Left:** Values of the FUV field derived from the HIRES 60, and 100 μm fluxes as color map. The strong, dashed contours correspond to values of $\chi = 1000, 2000,$ and 5000 in units of the Draine field. Overlaid in thin contours is the NANTEN2 CO 4–3 map. The central OB cluster is marked by a star. The two pillar heads are denoted by the squares. **Right:** Spitzer/IRAC 5.8 μm observation (in MJy/sr) overlaid with FUV fluxes as derived from IRAS/HIRES flux ratios. The contours correspond to values of $\chi = 2000, 3000, 4000,$ and 5000 . IRAC pixel size is 1.2". The boxes mark the position of the pillar heads. The crosses mark the positions along the cuts into MM1 and MM2.

4.3.2. FUV intensities

We use IRAS data to derive the FUV continuum in the observed region. To this end we obtained high resolution (HIRES) 60 and 100 μm images ($2^\circ \times 2^\circ$) from the IPAC data center². Enhanced resolution images of $\sim 1'$ resolution were created using the maximum correlation method (Aumann et al. 1990). Following Nakagawa et al. (1998), we combined these two data sets to create a map of far-infrared intensities between 42.5 μm and 122.5 μm (Helou et al. 1988). Under the assumption that the FUV energy absorbed by the grains is reradiated in the far-infrared (FIR), we then computed the FUV fluxes (χ) from the emergent FIR intensities (cf. Kramer et al. 2005) I_{FIR} , using $\chi/\chi_0 = 4\pi I_{\text{FIR}}$, with $\chi_0 = 2.7 \times 10^{-3} \text{ erg s}^{-1} \text{ cm}^{-2}$ (Draine 1978). The resulting map of the FUV continuum is shown in the left panel in Fig. 5. The dashed contours correspond to values of $\chi = 1000, 2000,$ and 5000 . Overlaid in thin contours is the NANTEN2 CO 4–3 map. The central OB cluster is marked by

a star. The two pillar heads are denoted by the squares. At the peak position of MM1, we find FUV fields of $\chi = 3460$. Along the cut in MM2, we find that χ gradually increases from 3350 at the position of the OB cluster to 5230 at the peak position. Due to the low spatial resolution of the HIRES data, these values are lower limits since beam dilution effects are not negligible.

To estimate upper limits for the total FUV flux, we consider the total luminosities of the most massive O stars in the central OB cluster. The most massive members of the OB cluster are 3 WNL stars, 6 O3 stars (III+V) and a dozen more O stars (Drissen et al. 1995). They produce the FUV flux that dominates the heating of the PDRs and the molecular clouds. At an effective temperature of 24000 K the ratio of the FUV energy density to the total energy density emitted by the star $\Phi_{\text{FUV}}/\Phi_{\text{tot}} \approx 0.7$ is maximal if we assume pure black body emission. At higher temperature relatively more energy is emitted in the EUV range ($13.6 \text{ eV} < h\nu < 130 \text{ eV}$). **Please note, that Pauldrach et al. (1998) showed in model calculations that for effective temperatures below 45000 K, the ratio of**

² <http://www.ipac.caltech.edu/>

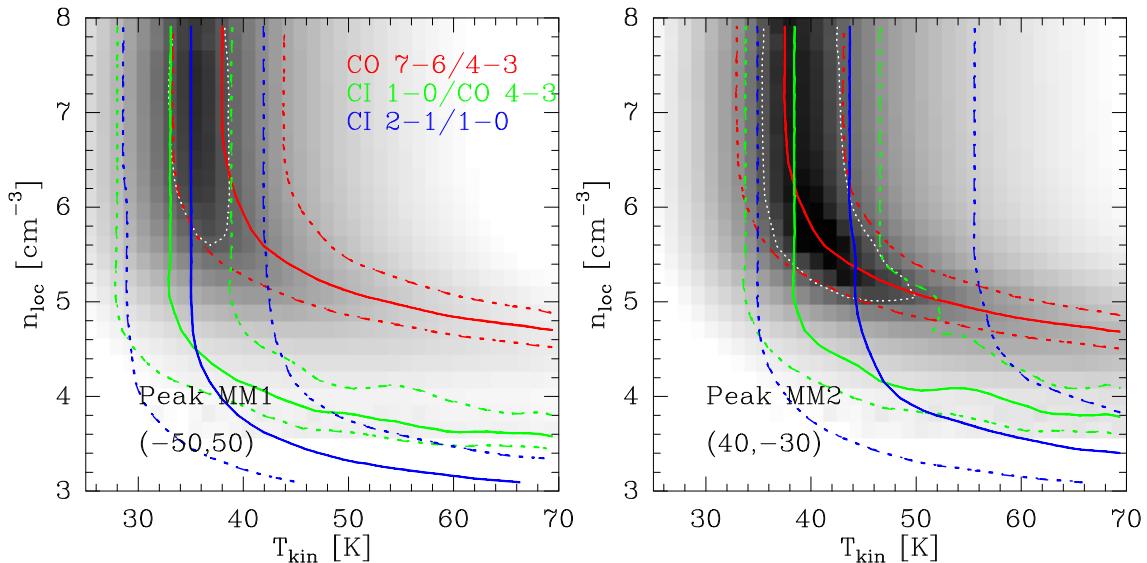


Fig. 6. Comparison of the observed line ratios $^{12}\text{CO}7-6/^{12}\text{CO}4-3$, $[\text{C I}]1-0/^{12}\text{CO}4-3$, and $[\text{C I}]2-1/[\text{C I}]1-0$ with results from an escape probability model at the peak positions of MM1 and MM2. The middle, solid contours represent the observed ratios, the outer dash-dotted contours represent the 20% uncertainties. The grey-scale image shows the reduced χ^2 of the fit. The white, dotted contours correspond to χ^2 values of 1, 2, and 5.

FUV to EUV photon rates is considerably higher than the ratio derived for pure blackbody spectra (see also Brandner et al. 2000). This is because EUV photons are absorbed in the ionization front. In the following we neglect this effect and assume pure blackbody characteristics.

Applying effective temperatures and luminosities as given by Panagia (1973) we calculated a total FUV luminosity of $2.4 \times 10^{40} \text{ erg s}^{-1}$ from the contribution of each cluster member. Depending on the distance from the cluster d , in units of pc, the FUV flux is $\chi = 7.2 \times 10^4 d^{-2}$. At a distance of 6 kpc, one parsec equals an angular distance of $34''$, i.e. somewhat smaller than the projected distance between the cluster and edge of MM2 as seen for example in Fig. 1 ($\approx 46''$). If we assume that the cluster and the molecular clouds are situated in the same plane the FUV field at the peak position in MM2 drops to $\chi \approx 7000$. This is of the same order as the flux at the MM2-peak derived from the IRAS data. However, an increasing FUV field towards the cluster cannot be seen in Fig. 5. Obviously, we expect the peak of molecular emission to be further away from the cluster than the interface region. Consequently, the FUV field should drop along the cut into MM2. Fig. 5 shows the opposite. One reason is the low resolution of the HIRES maps. Beam sizes vary from $\sim 33''$ to over $120''$ across the maps, hence the FUV values in Fig. 5 might be considerably beam diluted. In the right panel in Fig. 5 we overlaid the FUV fields derived from the HIRES data on $5.8\mu\text{m}$ Spitzer/IRAC observations of NGC 3603 to illustrate the beam filling effect: 60 and $100\mu\text{m}$ emission can only be measured if dust is present at all. The Spitzer map shows no dust emission between the interface and the cluster. The HIRES beam size at the cluster position is almost circular with a FWHM of $\sim 35''$. Hence the only contribution to the IRAS/HIRES fluxes at the cluster position can come from

the interface regions of MM1 and MM2. Even so, the beam dilution is significant and the derived FUV fluxes at the cluster position are a factor 20 smaller than the estimates from the spectral types. At the MM2-peak the beam is almost fully filled and the FUV fluxes are consistent with the assumption that the molecular cloud and the cluster lie in almost the same plane. This also supports the assumption that the FUV irradiation of the OB cluster created the pillars seen in the HST/VLT images.

The derived FUV flux can be used to estimate the ratio $I_{\text{CII}}/I_{\text{FUV}}$, i.e. the fraction of FUV energy that is reemitted in the the $[\text{CII}] 158\mu\text{m}$ cooling line. We retrieved the $[\text{CII}]$ spectrum from the ISO data archive³ and compute an integrated intensity of $2 \times 10^{-3} \text{ erg s}^{-1} \text{ cm}^{-2} \text{ sr}^{-1}$. Most of the FUV energy that irradiates the cloud is reradiated in the continuum, but a small fraction is reemitted in cooling lines, as the $[\text{CII}] 158\mu\text{m}$ line. Applying the FUV flux derived from the HIRES data, we estimate $I_{\text{CII}}/I_{\text{FUV}} \approx 0.2..0.3\%$. This is consistent with similar results from regions of active star formation, e.g. nuclear regions of galaxies, where approximately 0.1 to 1 % of the total FUV input is reradiated in the $[\text{CII}]$ line (Stacey et al. 1991). However this remains a rough estimate because of the large beam sizes.

We conclude that that the FUV flux, efficiently illuminating the molecular clumps MM1 and MM2 ranges between 2×10^4 (from the FUV radiation of the cluster members) and 5×10^3 (from the FIR data) in units of the Draine field. Approximately 0.2 to 0.3% of the total FUV energy is reemitted in the $[\text{CII}] 158\mu\text{m}$ cooling line.

³ <http://isowww.estec.esa.nl/ida/>

4.3.3. Escape Probability – density and temperatures

In Figure 6 we show a comparison of the observed line ratios R_{74} , R_{14} , and R_{21} with results from an escape probability (EP) model at the peak positions of MM1 and MM2. (REF EP STUTZKI et al. ?????)(ONE SENTENCE ON EP MODEL) **We assumed a CO:C abundance ratio of 10:1, consistent with the values from Table 2.** The solid contours represent the observed ratios, the dash-dotted contours flanking the solid contours represent 20% uncertainties. The grey-scale image shows the χ^2 of the fit:

$$\chi^2 = \sum_{i=1}^3 \left(\frac{R_i^{obs} - R_i^{mod}}{\sigma_i} \right)^2 \quad (1)$$

with the observed and modelled line ratios R_i^{obs} , and R_i^{mod} and the error σ_i which we assumed to be 20% for all ratios. The white, dotted contours correspond to χ^2 values of 5. At both positions the escape probability model gives a good constraint on the kinetic temperatures which are 35, and 40 K for MM1 and MM2, respectively. These temperatures are in good accord with the temperatures calculated under the assumption of LTE. It is not possible to reasonably constrain the gas density from EP analysis. The region of minimum χ^2 is very shallow and the numerical values of the particular absolute minima are not very significant given the overall uncertainties. Even so, it is possible to estimate lower limits for the gas densities. Figure 6 shows that we expect densities of $n \geq 10^{5.5} \text{ cm}^{-3}$ and $n \geq 10^5 \text{ cm}^{-3}$ for the peak positions of MM1 and MM2 respectively. **The high density for MM1 is consistent with the analysis of Nürnbergger et al. (2002) who derived a larger total column density than that of MM2 (1×10^{23} vs. $0.8 \times 10^{23} \text{ cm}^{-2}$) but much smaller spatial sizes ($R_{MM1} = 0.4 \text{ pc}$, $R_{MM2} = 1 \text{ pc}$). Using the LTE column densities from Table 2, a density of 10^5 cm^{-3} translates into spatial sizes of 0.2 pc, or 6'' in the distance of NGC 3603. However, the IRAC maps show much larger spatial sizes of approximately 100'' for MM2. Assuming a homogenous density of 10^5 cm^{-3} would imply a much too large total column density of $\approx 10^{24} \text{ cm}^{-2}$. This is a strong indication for a very clumpy density structure along the line of sight. The application of clumpy PDR models to the observations will be presented in another paper.**

5. Summary

We used the NANTEN2-4m telescope to, map the emission of atomic carbon and CO in the vicinity of the central OB cluster in the Galactic star forming region NGC 3603. These data are the first observations of CO 4–3, CO 7–6, CI 1–0, and CI 1–0 in NGC 3603, with simultaneously observed CO 7–6 and CI 2–1 lines. We presented the fully sampled $200'' \times 200''$ maps integrated over the full velocity range as well as channel maps of the CO 4–3 transition. The observed field includes the central OB cluster position as well as the two adjacent molecular clouds MM1 and MM2 hosting two pillar-like formations observed by the HST and similar in appearance to the famous pillar structures in the M16. We selected two cuts from the

OB cluster position to the peak emission in MM1 and MM2. The spectra along the two cuts show a rich kinematic structure, especially in MM2. The observed maps show the very strong correlation between the spatial distribution of C and CO. This implies either a face-on configuration of the clouds, i.e. both clouds being not in the same plane as the OB cluster and thus being illuminated face-on, or a more complex configuration, for instance a clumpy composition of many small clumps.

Assuming LTE we derived excitation temperatures for both clouds from the observed line ratios. The temperature derived from LTE are 26 K and 47 K for the peak positions of MM1 and MM2 respectively. Assuming optically thin emission we find column densities of atomic carbon of 1.5 and $4.2 \times 10^{17} \text{ cm}^{-2}$ in MM1 and MM2. Taking into account the C^{18}O 2–1 observation presented by Nürnbergger et al. (2002) we can derive total column densities of $1.6 \times 10^{22} \text{ cm}^{-2}$ and $2 - 5 \times 10^{22} \text{ cm}^{-2}$ for MM1 and MM2, i.e. an observed ratio of $\text{N(C)}/\text{N}$ of $8-9 \times 10^{-6}$. Using an escape probability model we derive lower limits for the local gas densities of $n \geq 10^{5.5} \text{ cm}^{-3}$ and 10^5 cm^{-3} in MM1 and MM2.

We used HIRES/IRAS far-infrared data to narrow down the value of the FUV field at the positions of the two molecular clouds. Consistent with estimates from spectral type approximations and with [CII] observations by ISO we find $\chi \approx 5 - 20 \times 1034$ in units of the Draine field.

Further observations with APEX and Herschel will provide the data to further study the physical and chemical conditions in NGC3603.

Acknowledgements. We made use of the NASA/IPAC/IRAS/HIRES data reduction facilities. Data reduction of the spectral line data was done with the *gildas* software package supported at IRAM (see <http://www.iram.fr/IRAMFR/GILDAS>).

This work is financially supported in part by a Grant-in-Aid for Scientific Research from the Ministry of Education, Culture, Sports, Science and Technology of Japan (No. 15071203) and from JSPS (No. 14102003 and No. 18684003), and by the JSPS core-to-core program (No. 17004). This work is also financially supported in part by the grant SFB494 of the Deutsche Forschungsgemeinschaft, the Ministerium für Innovation, Wissenschaft, Forschung und Technologie des Landes Nordrhein-Westfalen and through special grants of the Universität Bonn and Universität zu Köln.

References

- Aumann, H., Fowler, J., & Melnyk, M. 1990, AJ, 99, 1674
- Brandner, W., Grebel, E. K., Chu, Y.-H., et al. 2000, AJ, 119, 292
- Draine, B. T. 1978, ApJS, 36, 595
- Drissen, L., Moffat, A. F. J., Walborn, N. R., & Shara, M. M. 1995, AJ, 110, 2235
- Frerking, M. A., Langer, W. D., & Wilson, R. W. 1982, ApJ, 262, 590
- Gorti, U. & Hollenbach, D. 2002, ApJ, 573, 215
- Goss, W. M. & Radhakrishnan, V. 1969, Astrophys. Lett., 4, 199
- Grabelsky, D. A., Cohen, R. S., Bronfman, L., & Thaddeus, P. 1988, ApJ, 331, 181

- Helou, G., Khan, I., Malek, L., & Boehmer, L. 1988, *ApJ*, 68, 151
- Ikeda, M., Oka, T., Tatematsu, K., Sekimoto, Y., & Yamamoto, S. 2002, *ApJS*, 139, 467
- Kramer, C., Mookerjee, B., Bayet, E., et al. 2005, *A&A*, 441, 961
- Kramer, C., Yonekura, Y., Röllig, M., et al. 2007, *A&A*
- Müller, H. S. P., Schlöder, F., Stutzki, J., & Winnewisser, G. 2005, *Journal of Molecular Structure*, 742, 215
- Müller, H. S. P., Thorwirth, S., Roth, D. A., & Winnewisser, G. 2001, *A&A*, 370, L49
- Nakagawa, T., Yui, Y. Y., & Doi, Y., et al. 1998, *ApJS*, 115, 259
- Nürnberg, D. E. A., Bronfman, L., Yorke, H. W., & Zinnecker, H. 2002, *A&A*, 394, 253
- Panagia, N. 1973, *AJ*, 78, 929
- Pardo, J., Cernicharo, J., & Serabyn, E. 2001, *IEEE Transactions on Antennas and Propagation*, 49, 1683
- Pauldrach, A. W. A., Lennon, M., Hoffmann, T. L., et al. 1998, in *Astronomical Society of the Pacific Conference Series*, Vol. 131, *Properties of Hot Luminous Stars*, ed. I. Howarth, 258–+
- Sakai, J. I., Nagasugi, Y., Saito, S., & Kaufmann, P. 2006, *A&A*, 457, 313
- Simon, R., Graf, U., Kramer, C., Stutzki, J., & Onishi, T. 2007, *NANTEN technical report*, 13.2.2007, 1, 1
- Stacey, G. J., Geis, N., Genzel, R., et al. 1991, *ApJ*, 373, 423
- Stolte, A., Brandner, W., Brandl, B., & Zinnecker, H. 2006, *AJ*, 132, 253
- Stolte, A., Brandner, W., Brandl, B., Zinnecker, H., & Grebel, E. K. 2004, *AJ*, 128, 765
- Tatematsu, K., Jaffe, D. T., Plume, R., Evans, II, N. J., & Keene, J. 1999, *ApJ*, 526, 295